Journal of ELECTRONIC MATERIALS, Vol. 47, No. 2, 2018
DOI: 10.1007/s11664-017-5874-1

Effects of Starting Precursor Ratio on Optoelectrical Properties and Blue Emission of Nanostructured C-ZnS Thin Films Prepared by Spin Coating

N. RAHIMZADEH,[1] F.E. GHODSI,[1,2] and J. MAZLOOM[1]

1.—Department of Physics, Faculty of Science, University of Guilan, Namjoo Avenue, P.O. Box 413351914, Rasht, Iran. 2.—e-mail: feghodsi@guilan.ac.ir

Nanocrystalline cubic zinc sulfide (C-ZnS) thin films have been elaborated by sol–gel spin-coating of Zn(Ac)/thiourea starting precursors at different molar ratios, and their structural, morphological, compositional, optical, electrical, and photoluminescence properties comprehensively investigated. x-ray diffraction results showed that the samples had dominant cubic structure and their crystallinity improved with increasing S content. Morphological characterization of the C-ZnS thin films was carried out by field-emission scanning electron microscopy (FESEM), revealing that the films were smooth with spherical grains included in clusters. Energy-dispersive x-ray and Fourier-transform infrared spectra of ZnS compounds did not show any evidence of impurities. Optical characterization revealed increases of the average optical transmittance and bandgap (from 3.2 eV to 3.56 eV) with increasing S content. The refractive index in the visible region increased with the S content, while the extinction coefficient decreased. The compositional dependence of the optical dispersion parameters (oscillator and dispersion energy), dielectric constant, and surface energy loss function of the films was evaluated. Electrical characterization of the films was carried out using Hall-effect measurements. The ZnS thin films exhibited *n*-type conductivity, and the electrical resistivity decreased with increasing carrier concentration and mobility due to enhanced crystallite size and reduced structural disorder. Photoluminescence (PL) measurements indicated a blue-shift of the near-band-edge emission. The blue emission peaks centered at about 438 nm and 487 nm were enhanced due to transitions involving interstitial S atoms, surface states, and zinc vacancies.

Key words: ZnS thin film, sol–gel, optical properties, electrical mobility, blue emission

INTRODUCTION

Semiconductor nanocrystals, particularly quantum dots (QDs), have attracted much attention in recent years due to their unique physical and chemical properties which differ from those of bulk materials.[1–4] In particular, synthesis of II–VI compounds, which exhibit the quantum size effect, has attracted a great deal of attention over the last decade. Zinc sulfide (ZnS) is an important *n*-type II–VI compound with wide direct bandgap (3.5 eV to 3.7 eV) at room temperature,[5] relatively high refractive index,[6] and high transmittance[7,8] in the visible range. In Nature, it is observed in two crystalline phases: zincblende cubic phase (C-ZnS) and wurtzite hexagonal phase (H-ZnS). C-ZnS is more stable at low temperatures and atmospheric pressure, transforming to H-ZnS only at ≥ 1023°C.[9,10] ZnS has been studied extensively

(Received June 30, 2017; accepted October 10, 2017; published online October 30, 2017)

owing to its potential applications and novel physical and electronic and excellent luminescence and photochemical properties.[11–16] It is used in thin-film technology such as luminescent and electroluminescent devices, photodetectors, biosensors, light-emitting displays, flat-panel displays, light-emitting diodes, and dielectric filters. It is a promising material for use in future applications such as window layers in solar cells, data storage, data transfer, and ultraviolet (UV)-sensitive coatings.[5,17–26]

Zinc sulfide thin films have been investigated as alternative buffer layers to CdS for use in copper indium gallium selenide (CIGS) and cadmium telluride (CdTe) thin-film solar cells. Despite the higher efficiency of solar cells using CdS ($\sim$ 19.5%) compared with CIGS solar cells with ZnS ($\sim$ 18.6%), use of CdS results in toxic hazards. This has stimulated research towards development of Cd-free buffer layers. Moreover, solar cells with a ZnS window layer are expected to show higher photocurrent in the blue wavelength region of the solar radiation spectrum because of its higher bandgap compared with CdS.[6,7,20,27–30]

ZnS thin films can be deposited using several methods. Besides physical methods such as sputtering[31] and pulsed laser deposition,[32] there are also a number of chemical methods, including chemical bath deposition (CBD),[5–7,28] chemical vapor deposition (CVD),[33] spray pyrolysis,[34] and sol–gel.[35] Chemical methods offer the significant advantage that they can lead to mass production with high output efficiency at moderate cost, while their main drawback is a lack of phase purity, which is difficult to control at large scale.[22]

Many parameters affect the physical properties of ZnS thin films obtained by the sol–gel method, including annealing temperature,[35] sulfide treatment,[21] compositional ratio,[36] etc. The effect of the sintering temperature and precursor composition on sol–gel deposition of ZnS (O,OH) was investigated by Bu.[35] ZnS(O,OH) films were crystallized at temperature above 500°C. Nevertheless, they only showed hexagonal ZnO structure, and only a weak peak corresponding to H-ZnS (002) appeared under excess S precursor condition with a mixture of ZnO peaks. As a result, pure ZnS structure was not found in that research. Lin and Ni[21] investigated the effects of sulfide treatment on the electrical, photoluminescent, and structural properties of ZnS films deposited by sol–gel method. They found that the *p*-type conductivity of the films resulted from sulfide treatment. In another study, Nilkar et al.[36] deposited ZnS–SiO_2 nanocomposite films by sol–gel dip-coating technique, finding that the crystallinity of the films was improved according to x-ray diffraction (XRD) patterns on increasing the ZnS concentration in the composite thin films. To the best of the authors' knowledge, the present study is the first on the effects of the starting precursor ratio on the optical constants, electrical conductivity, and photoluminescence (PL) emission of cubic ZnS thin film deposited by spin-coating technique. In recent decades, numerous theoretical approaches have also been presented to determine physical and chemical properties of zinc sulfide, leading to interesting results. These studies have led to a broader view of the physical and chemical properties of zinc sulfide.[37–40]

In the present study, we prepared nanostructured ZnS thin films by sol–gel spin-coating technique. The samples were prepared in various conditions (zinc-rich, equimolar zinc and sulfur, and sulfur-rich mixture) and analyzed comprehensively to determine the optimum values of the ZnS film. Despite the large amount of research on ZnS, most reports have focused on structural and morphological properties, while there is a lack of systematic studies on the optical, electrical, and photoluminescence properties of ZnS thin films. Therefore, we specifically focus on the electrical, photoluminescence, and optical properties as well as structural and morphological properties of the ZnS thin films.

EXPERIMENTAL PROCEDURES

Film Preparation

ZnS thin films were prepared by sol–gel method using zinc acetate dihydrate [$Zn(CH_3COO)_2{\cdot}2H_2O$, 98%] and thiourea [$SC(NH_2)_2$, 99.98%] as starting precursors, with 2-methoxyethanol and monoethanolamine (MEA) as solvent and stabilizer, respectively. Three types of sol (0.5 M) were synthesized with different molar ratios of initial precursors Zn(Ac)/thiourea of 2/1, 1/1, and 1/2 in 2-methoxyethanol and monoethanolamine. The molar ratio of MEA to zinc acetate was kept constant at 1. All solutions were stirred at 60°C for 30 min, then stirred constantly at room temperature for 1 h to obtain homogeneous solution. The final solutions were then aged for 24 h to obtain clear solutions. Films were deposited on glass substrates by spin-coating technique. Prior to deposition, the glass substrates were first degreased using detergent, rinsed thoroughly using deionized water, then cleaned ultrasonically in a mixture of ethanol and acetone (each 50% by volume) for 15 min to remove macroscopic contamination. Finally, the substrates were immersed in acetone and dried under nitrogen flow. Clear and transparent sols were coated on glass substrates by spin-coating method at speed of 3200 rpm. Next, the coated glass substrates were dried at 170°C for 15 min and the coating–drying procedures repeated seven times to yield films of desired thickness. Finally, the dried films were annealed at 500°C for 1 h in Ar atmosphere.

Characterization

The structural properties of the samples were investigated by x-ray diffractometer (Philips PW-1840) with Cu K_α radiation (λ_{CuK_α} = 0.15406 nm).

An Alfa Bruker Fourier-transform infrared (FTIR) spectrometer was used to identify the molecular bonds in the samples. The surface morphology of the films was characterized by field-emission scanning electron microscopy (FESEM) using a Mira 3-XMU TESCAN instrument. Energy-dispersive spectroscopy analysis was carried out within the same FESEM chamber. To study the optical characteristics of the deposited films, transmission spectra were measured using a Varian Cary 100 UV–Vis spectrophotometer. Electrical measurements were carried out using the van der Pauw technique and a Hall-effect measurement system (RH2010). Finally, a PerkinElmer (LS-55) fluorescence spectrometer was utilized to record the photoluminescence (PL) spectra of the prepared films at excitation wavelengths of 245 nm and 356 nm.

RESULTS AND DISCUSSION

Structural and Molecular Properties

The x-ray diffraction patterns of the films prepared using different Zn/S molar ratios are presented in Fig. 1. In all the XRD patterns, the prominent diffraction peak located at $2\theta = 28.5°$, associated with (111) plane, can be well indexed to standard data for ZnS with cubic structure in Joint Committee on Powder Diffraction Standards (JCPDS) card no. 05-0566. This result is inconsistent with data provided by Bu,[35] who obtained hexagonal ZnS thin films using sol–gel spin-coating technique. It is clear that the Zn/S = 2/1 sample exhibited an additional peak corresponding to (002) plane that matched with hexagonal ZnO crystal structure, due to addition of excess Zn.[35] In the XRD pattern of the ZnS = 1/1 sample, no peak corresponding to hexagonal phase of ZnO was detected, but the (111) and (220) peaks were not strong enough to be attributed to the cubic structure of ZnS. Finally, the XRD pattern of the Zn/S = 1/2 sample showed a moderate rise in the sharpness of ZnS (111), (220), and (311) peaks. Furthermore, these peaks became narrower, indicating better crystallinity of this latter sample (ZnS = 1/2). To study the effect of the ratio of starting precursors on the crystallite size of the prepared films, the average crystallite size of the samples was calculated using Scherrer's formula:

$$D = \frac{k\lambda}{\beta \cos\theta}, \qquad (1)$$

where D is the average crystallite size, K is the shape factor, which is a constant, λ is the Cu K_α x-ray wavelength (1.5406 Å), β is the full-width at half-maximum (FWHM) of the diffraction peaks, and θ is Bragg's diffraction angle. The calculated average crystallite size is presented in Table I. It was found that the crystallite size increased from 4.2 nm to 5.4 nm as the sulfide content was increased. All of the observed peaks could be attributed to ZnS with cubic structure (JCPDS no. 05-0566) with lattice constant of 5.406 Å. This value is very close to the lattice constant reported in Table I.

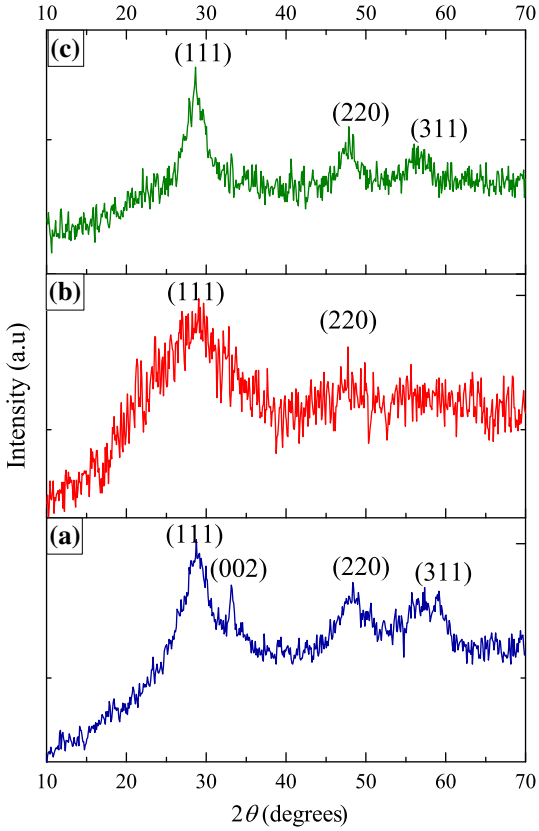

Fig. 1. XRD patterns of ZnS thin films obtained using different Zn/S molar ratios: (a) 2/1, (b) 1/1, and (c) 1/2.

To investigate the functional groups and chemical bonds, Fourier-transform infrared (FTIR) spectra of ZnS samples with different Zn/S molar ratios annealed at 500°C were recorded in the wavenumber range from 4000 cm^{-1} to 400 cm^{-1}, as shown in Fig. 2. The presence of hydroxyl (–OH) group was noticed based on a broad band centered at around 3419 cm^{-1} and a sharp peak at 1625 cm^{-1}, corresponding to vibration and bending mode of water molecules due to presence of moisture in the samples.[28,41] The intensity of the peaks decreased with increasing S molar ratio. Moreover, the absorption bands observed in the range from 2028 cm^{-1} to 2361 cm^{-1} were attributed to C–O stretching modes arising from absorption of atmospheric CO_2 on the surface.[8,41] The principal absorption peaks centered at 1409 cm^{-1} were due to asymmetric and symmetric stretching vibration of COO– bond, indicating that acetate group from the zinc acetate precursor used for zinc ions remained in the synthesized nanoparticles.[8,24,42] Furthermore, the peak at 1024 cm^{-1} split into two peaks at 1050 cm^{-1} and 1103 cm^{-1} for the sample obtained using molar ratio of Zn/S = 1/2, being

Table I. Structural parameters of samples prepared using different Zn/S molar ratios

Zn/S	FWHM, β (rad)	2θ (rad)	D (nm)	Lattice constant (Å)
2/1	1.95	28.85	4.2	5.35
1/1	1.82	28.59	4.5	5.40
1/2	1.51	28.63	5.4	5.39

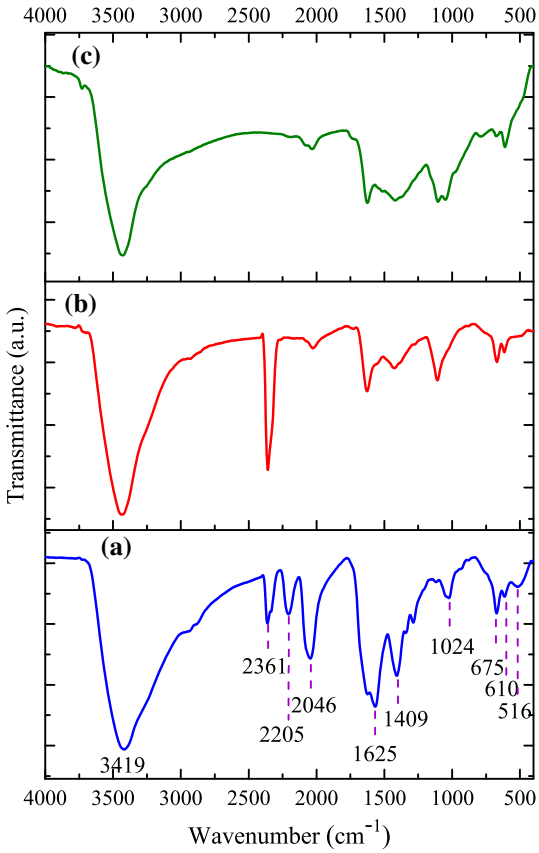

Fig. 2. FTIR spectra of ZnS thin films obtained using different Zn/S molar ratios: (a) 2/1, (b) 1/1, and (c) 1/2.

attributed to deformation bands of C–O.[8] The peak observed at 516 cm^{-1} was attributed to ZnO vibrations,[43] and those in the range from 610 cm^{-1} to 675 cm^{-1} as due to Zn–S stretching vibration, being assigned to the ZnS band (corresponding to sulfides).[25,42,44,45] As is evident from Fig. 2, with increasing S content, the first aforementioned band disappeared while the intensity of the latter was enhanced.

Morphological and Compositional Characterization

The morphology of the ZnS thin films was studied by FESEM, as shown in Fig. 3. Overall, the surface of the samples was homogeneous and crack free, but it was obvious that all the ZnS thin films exhibited spherical morphology of various sizes. Uniform size and quite good dispersibility of the particles were achieved at Zn/S molar ratio of 1/2. With increasing amount of thiourea, the concentration of S^{2-} increased and the size of the grains decreased. Moreover, in Fig. 3b, several grains are observed in cluster form, distributed randomly, while in Fig. 3a, the agglomeration of grains increased and the grain size enhanced slightly.

The elemental composition of the ZnS thin films was investigated by energy-dispersive x-ray (EDX) analysis, as shown in Fig. 4. The EDX spectrum of the films revealed that the films contained Zn, Si, O, Ca, and S elements without any impurities. The presence of Si and Ca elements is typically expected due to the use of glass substrate. Consequently, the signals from the other elements indicate the exact composition of the films. It can be seen that the intensity of Zn and O peaks decreased slightly in Fig. 4b with increasing S molar ratio.

Optical Properties

To investigate the optical properties, the transmittance spectra of all films were measured and optical parameters such as the refractive index (n), extinction coefficient (k), and bandgap (E_g) analyzed based on the spectral data. Figure 5 presents the optical transmission spectra for the ZnS thin films obtained using different Zn/S molar ratios in the range from 300 nm to 800 nm. It is clear that all the films were highly transparent with average transmittance in the visible range of around $\sim$ 79% to 84%. The appearance of interference fringe patterns in the transmission spectra in the transparent region provides evidence that the film surface was smooth, in good agreement with the FESEM results above. In addition, these results reveal that, with increasing S content in the ZnS thin films, the absorption edge shifted to lower wavelength, resulting in blue-shift of the absorption edge.

The optical properties of the films were evaluated from the transmittance data using the method proposed by Swanepoel.[46] To calculate the refractive index (n) in the transparent region, the following formula can be used:

$$n = \left[N + (N^2 - S^2)^{\frac{1}{2}}\right]^{\frac{1}{2}}, \quad (2)$$

where N is defined as

$$N = 2s\frac{T_M - T_m}{T_M T_m} + \frac{s^2 + 1}{2}, \quad (3)$$

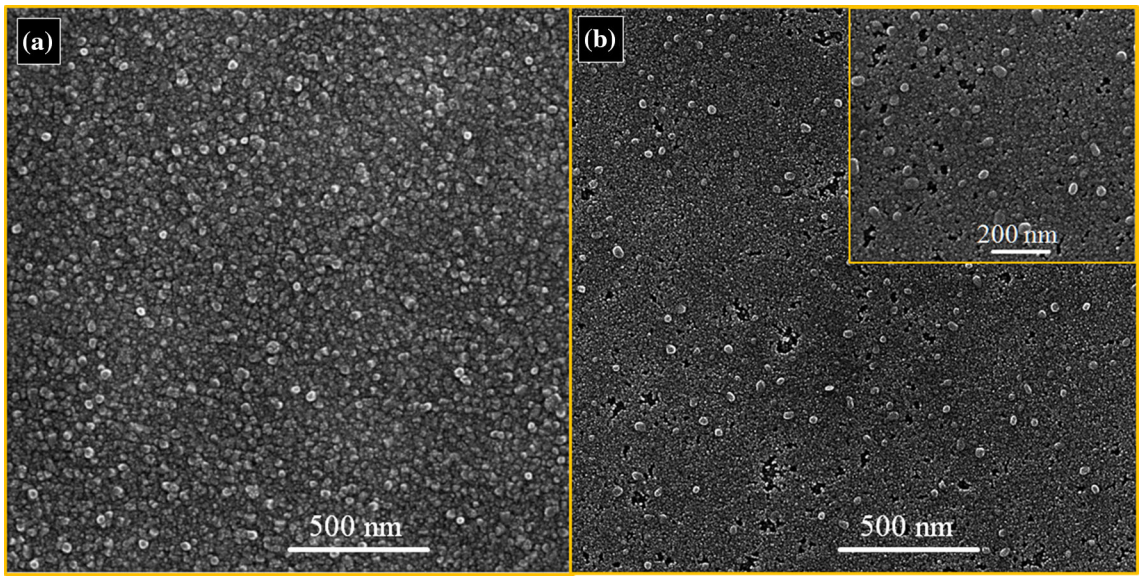

Fig. 3. FESEM of ZnS thin films obtained using different Zn/S molar ratios: (a) 1/1 and (b) 1/2.

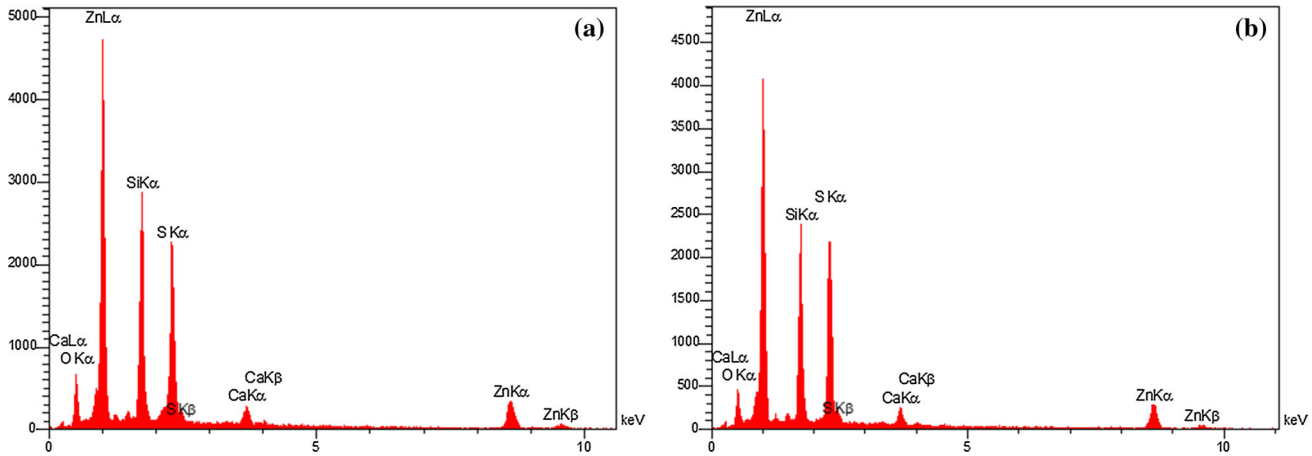

Fig. 4. EDX results for ZnS thin films obtained at Zn/S molar ratio of (a) 1/1 and (b) 1/2.

where T_M and T_m are taken from the peaks and valleys of the envelope curves of the transmittance spectrum, respectively, and s is the refractive index of the substrate.

The n and k values obtained for the films were fit using the Cauchy formula[47] and are shown in Figs. 6 and 7, respectively. The refractive index values showed normal dispersion behavior in the visible region and increased with increasing S content in the ZnS thin films, in good agreement with some theoretical results.[37,38] For the Zn/S = 2/1 sample, the refractive index was close to that of ZnO material, whereas the refractive index obtained for the Zn/S = 1/2 sample was equal to that of ZnS material.[48]

These results reveal that the refractive index of the films depended on the mixing ratio as well as the microstructure. Furthermore, the decrease in the extinction coefficient of the films with increasing thiourea content in the initial sol is confirmed by the enhancement of the transmission spectra in the visible region and can be attributed to the decreased thickness of the films.

The thickness of the films was also determined from the calculated n values using a simple graphical method. Figure 8 shows a plot of $l/2$ versus n/λ. The slopes of the best-fit lines on the graphs yield values for $2d$, according to the equation[46]

$$\frac{l}{2} = 2d\left(\frac{n}{\lambda}\right) - m_0 \quad \text{and} \quad l = 0, 1, 2, \ldots \tag{4}$$

The film thickness decreased from 905 nm to 462 nm with increasing S content in the Zn/S molar ratio (Table II).

The value of the direct allowed optical bandgap (E_g) of the thin films was determined from the

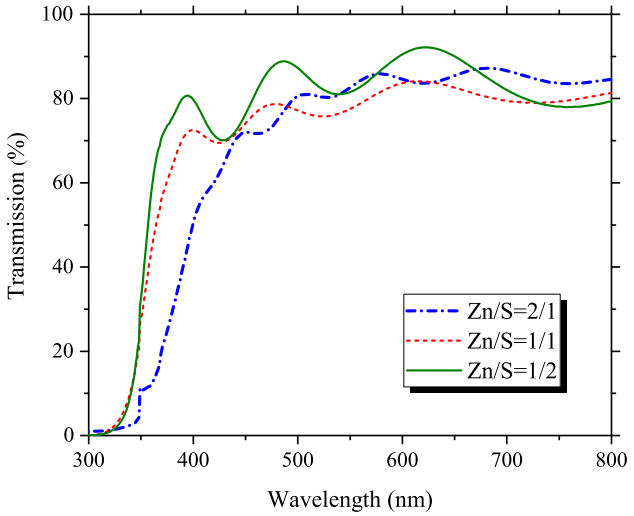

Fig. 5. Transmission spectra of ZnS thin films obtained using different Zn/S molar ratios.

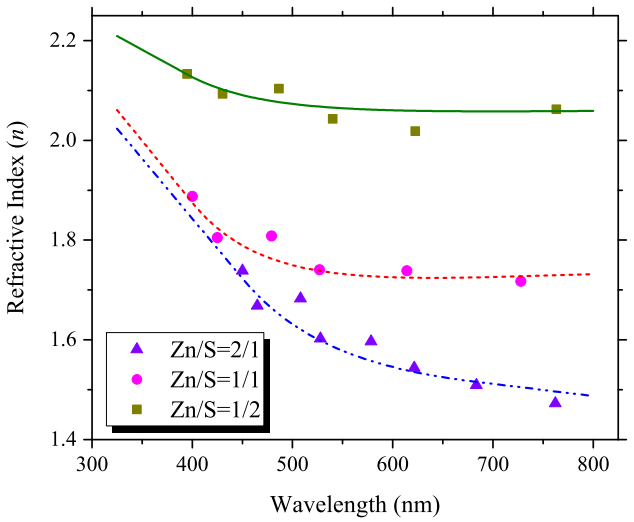

Fig. 6. Refractive index, n, of ZnS thin films as function of wavelength.

optical absorption coefficient (α) by using Tauc's relationship[49]:

$$(\alpha h\upsilon) = A(h\upsilon - E_g)^{\frac{1}{2}}, \quad (5)$$

where $h\upsilon$ is the photon energy and A is a constant. To calculate the optical absorption coefficient, α, the following equation was used[46]:

$$x = \exp(-\alpha d). \quad (6)$$

The values of x were then calculated using the following equation[46]:

$$x = \frac{(n-1)^2(n+s^2)}{16n^2 s} T_0, \quad (7)$$

where n is the dispersion of the refractive index fit using the Cauchy formula, s is the refractive index

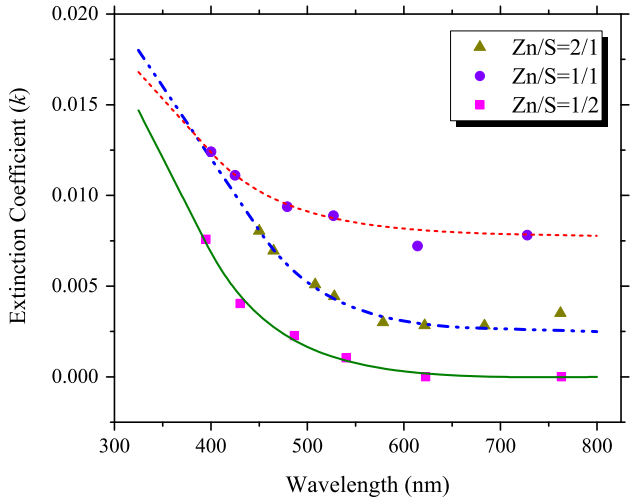

Fig. 7. Extinction coefficient, k, of thin films as function of wavelength.

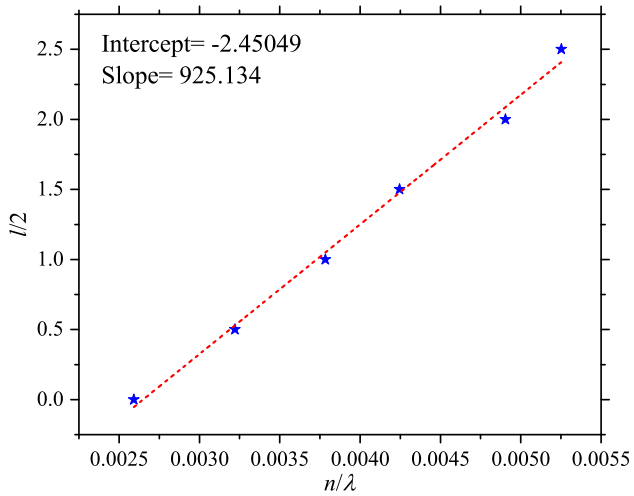

Fig. 8. $I/2$ versus n/λ plot for Zn/S = 1/2 thin film.

of the substrate, and T_0 is the transmission value in the strong absorption region. Figure 9 shows the variation of $(\alpha h\upsilon)^2$ versus photon energy. The optical bandgap was obtained by extrapolating the linear part of the $(\alpha h\upsilon)^2$ versus $(h\upsilon)$ graph to intercept the energy axis ($\alpha h\upsilon = 0$). The calculated values are reported in Table II. These results show that the bandgap widened with increasing S content in the Zn/S molar ratio, consistent with theoretical results.[37,39]

The dispersion of the refractive index for the films in the visible region was analyzed using the single-oscillator model proposed by Wemple–DrDomenico.[50] This model describes the relation between the refractive index n and the single-oscillator strength below the bandgap energy as

$$n^2 - 1 = \frac{E_0 E_d}{E_0^2 - E^2}, \quad (8)$$

Table II. Calculated optical parameters of ZnS thin films prepared using different Zn/S molar ratios

Zn/S	T_{avg} (%)	n	k	d (nm)	E_g (eV)	E_0 (eV)	E_0/E_g	E_d (eV)	M_{-1}	M_{-3} (eV)$^{-2}$
2/1	79.0	1.57	0.004	905	3.2	6.26	1.96	12.71	2.03	0.052
1/1	78.4	1.73	0.009	529	3.44	6.37	1.85	13.28	2.08	0.051
1/2	84.1	2.06	0.001	462	3.56	7.17	2.01	20.56	2.87	0.056

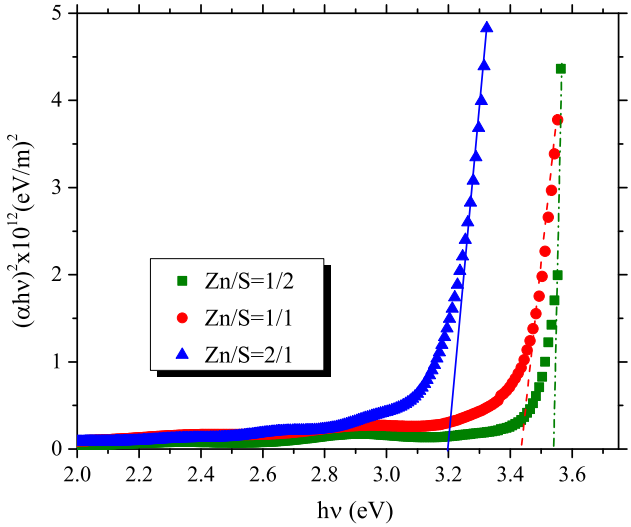

Fig. 9. $(\alpha h\nu)^2$ versus $h\nu$ for different Zn/S molar ratios.

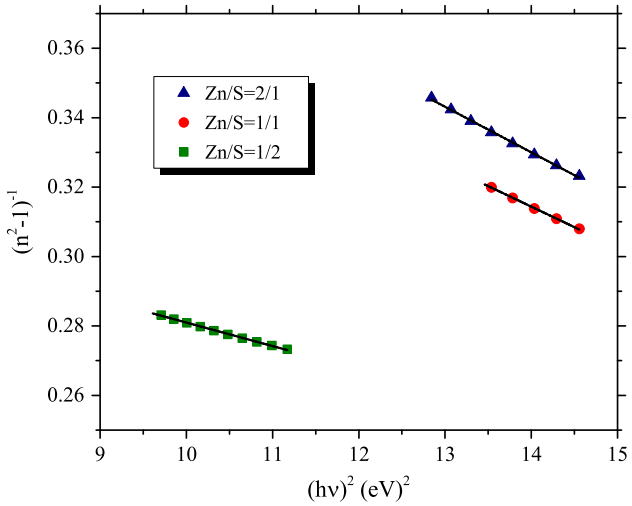

Fig. 10. $(n^2 - 1)^{-1}$ versus $(h\nu)^2$ for thin films obtained with different Zn/S molar ratios.

where E_0 is the single-oscillator energy, which can be considered as representing an average energy gap, and E_d is the dispersion energy, which evaluates the average strength of interband transitions. By plotting $(n^2 - 1)^{-1}$ versus E^2, experimental verification of Eq. 9 can be obtained. As shown in Fig. 10, E_0 and E_d were calculated from the slope $(E_0E_d)^{-1}$ and intercept (E_0/E_d) of the best linear fit, as given in Table II. As can be observed, E_0 and E_d increased with increasing S content, indicating that the probability of electronic transitions between electronic bands increased. The oscillation energy, E_0, can be attributed to the estimated optical gap according to the empirical formula $E_0 \simeq 2E_g$. In addition, the average bond strength was calculated by optical moments, M_{-1} and M_{-3}, from the E_0 and E_d data using the following relationships; their values are given in Table II[50]:

$$M_{-1} = \frac{E_d}{E_0}, \quad M_{-3} = \frac{E_d}{E_0^3}. \tag{9}$$

The polarizability of any solid is proportional to its dielectric constant $\varepsilon(\omega) = \varepsilon_r(\omega) + i\varepsilon_i(\omega)$. The real (ε_r) and imaginary (ε_i) parts of the complex dielectric constants of the Zn/S thin films were calculated using the following relations[51]:

$$\varepsilon_r(\omega) = n^2(\omega) - k^2(\omega), \ \varepsilon_i(\omega) = 2n(\omega)k(\omega). \tag{10}$$

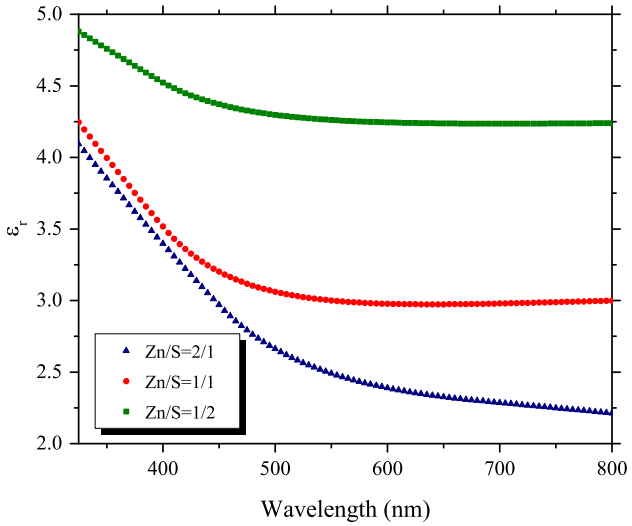

Fig. 11. Real component of complex dielectric constant as function of wavelength.

The variation of ε_r and ε_i of the ZnS nanocrystalline thin films obtained using different molar ratios are shown versus wavelength in Figs. 11 and 12, respectively. Both ε_r and ε_i decreased with increasing wavelength, and their values are well consistent with theoretical calculations.[37] The imaginary part for the films with molar ratio Zn/S = 2/1 and Zn/

S = 1/1 was higher than for the film with Zn/S = 1/2 molar ratio, indicating higher dielectric loss and higher absorption coefficient for these films.

The rate of energy loss for electrons passing through a material can be described within the framework of dielectric theory by the volume energy loss function (VELF) and surface energy loss function (SELF), which are related to the real and imaginary parts of the dielectric constant as follows[52]:

$$\mathrm{VELF} = -\mathrm{Im}\left(\frac{1}{\varepsilon^*}\right) = \frac{\varepsilon_\mathrm{i}}{\varepsilon_\mathrm{r}^2 + \varepsilon_\mathrm{i}^2}, \tag{11}$$

$$\mathrm{SELF} = -\mathrm{Im}\left(\frac{1}{\varepsilon^* + 1}\right) = \frac{\varepsilon_\mathrm{i}}{(\varepsilon_\mathrm{r} + 1)^2 + \varepsilon_\mathrm{i}^2}. \tag{12}$$

To calculate these quantities, the real and imaginary parts of the dielectric constant were used. Figure 13 shows the obtained results. It is clear that the energy loss occurring due to free charge carriers when traversing the bulk material exhibits fairly the same behavior as when traversing the surface, but the VELF plot increases more than the SELF plot for the ZnS thin films.

Photoluminescence Study of ZnS Thin Films

ZnS nanocrystals have high intrinsic photoluminescence (PL) quantum efficiency due to their direct band transitions.[53] Figures 14 and 15 show the PL spectra of ZnS thin films obtained using different values of Zn/S monitored at two excitation wavelengths, viz. 245 nm and 356 nm, respectively. Figure 14 clearly shows that the PL emission peak shifted from 410 nm to 375 nm as the sulfide content was increased. The peaks can be attributed to near-band-edge (NBE) emission, and this shift corroborates the blue-shift of the bandgap in the

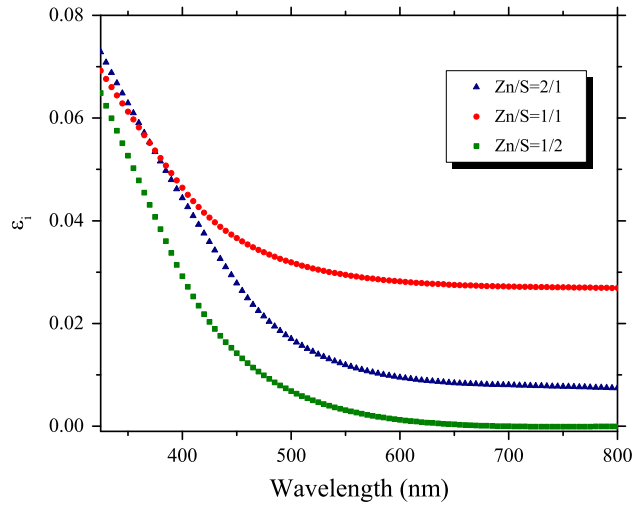

Fig. 12. Imaginary component of complex dielectric constant as function of wavelength.

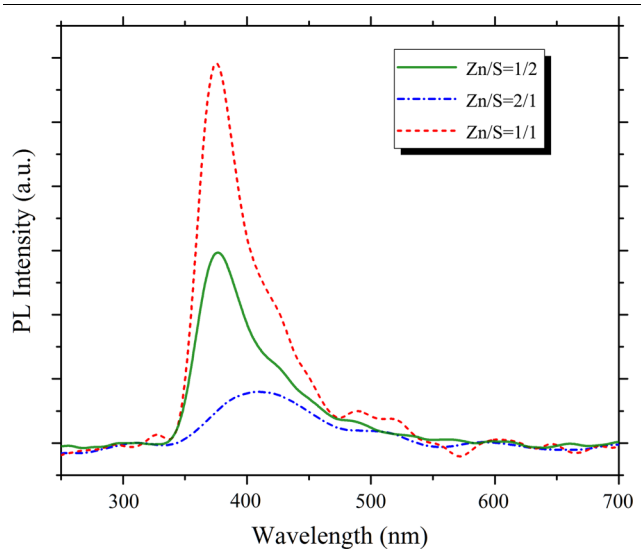

Fig. 14. PL spectra at excitation wavelength of 245 nm for ZnS thin films obtained using different Zn/S molar ratios.

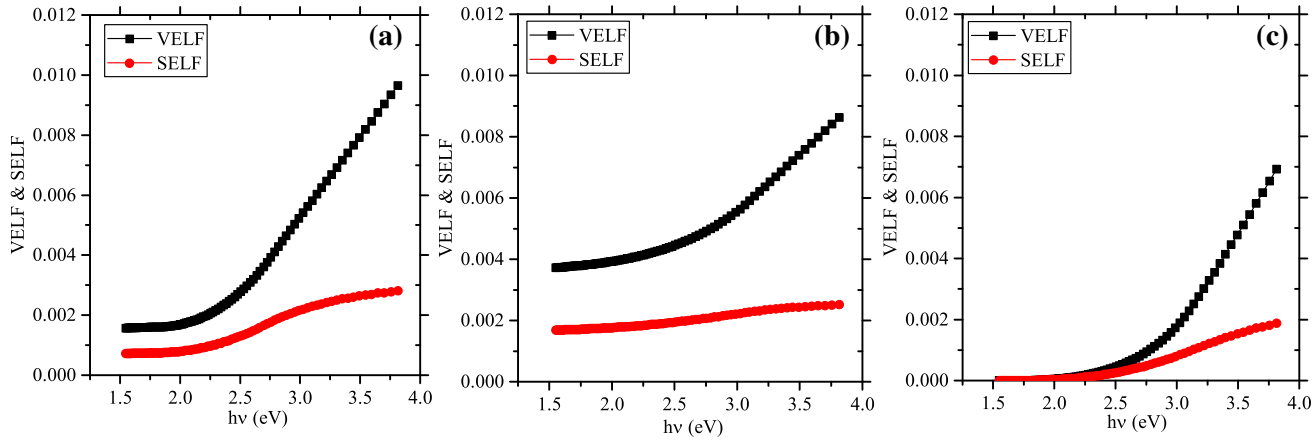

Fig. 13. VELF and SELF versus $h\nu$ for nanostructured ZnS thin films obtained with different Zn/S molar ratios: (a) 2/1, (b) 1/1, and (c) 1/2.

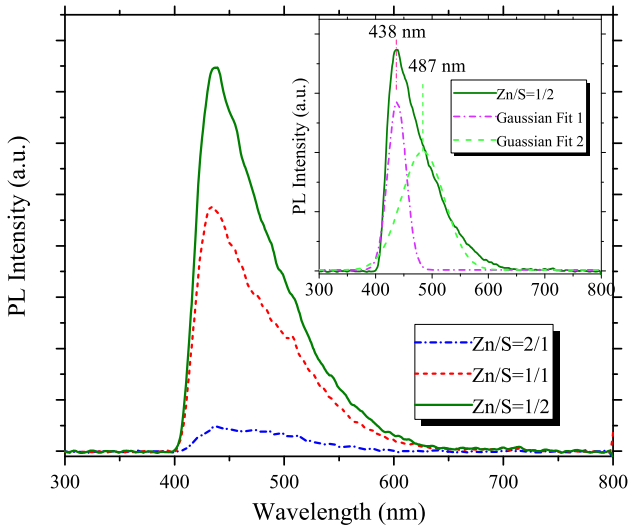

Fig. 15. PL spectra at excitation wavelength of 356 nm for ZnS thin films obtained using different Zn/S molar ratios; inset shows Gaussian fitting for determination of peak positions.

transmission spectra. Similar behavior was reported by Bu for H-Zn(O)S.[35]

Figure 15 shows the PL spectra of ZnS thin films obtained at excitation wavelength of 356 nm. The Gaussian dispersion model was used to deconvolute the emission peaks. Unlike previous PL results for Zn/S thin films, which showed only a single peak at 423 nm,[35] dual peaks at 438 nm and 487 nm were observed in our experiments. The asymmetric nature of the PL spectra with multiple peaks is due to the various native defect levels that may be present in the prepared ZnS thin films. According to their energies, the emission peaks can be attributed to various point defects as follows: Blue/violet emission centered at 438 nm of ZnS is assigned to interstitial S atoms, surface states, and zinc vacancies.[54–56] The blue emission at 487 nm can be attributed to zinc vacancies (V_{Zn}) in ZnS thin films.[57,58] Furthermore, the PL intensities were enhanced with increasing S content in the Zn/S thin films. Defects normally act as sites for nonradiative recombination of electron–hole pairs. So, higher crystallinity with low concentration of defects will benefit the emission intensities.[59]

Electrical Studies

The electrical resistivity (ρ), carrier concentration (n), and carrier mobility (μ) of the films were obtained using Hall-effect measurements in van der Pauw geometry at room temperature using silver ohmic contacts on the surface of the films in a magnetic field of $B = 0.9$ T. The results are presented in Table III. All the samples exhibited n-type conductivity regardless of the different molar ratios used, although this is in contrast to the results reported by Lin and Ni.[21] In addition, the results show that, with increasing sulfide content in the Zn/S molar ratio, the carrier concentration n and mobility μ increased. On the other hand, the resistivity of the films decreased from 7.78×10^4 Ω cm to 1.99×10^3 Ω cm as a result of the increase in free carrier concentration with enhancement of the S molar ratio in the Zn/S films. According to the XRD patterns, the lowest resistivity of the Zn/S = 1/2 thin film can be assigned to enhanced crystallite size and reduced structural disorder, which can lead to decreased electron scattering at grain boundaries and increased carrier mobility. In addition, the enhanced blue emission observed in the PL spectra confirms that the highest content of interstitial S atoms, surface states, and zinc vacancies in the sample with Zn/S = 1/2 caused the maximum carrier concentration for this sample.

CONCLUSIONS

Nanocrystalline zinc sulfide thin films were prepared on glass substrates by sol–gel spin-coating method. The effects of the initial precursor ratio on the structural, optical, PL emission, and electrical parameters were investigated. XRD patterns revealed that the films had cubic structure with (111) preferred orientation with an additional (002) peak appearing for the Zn/S = 2/1 sample due to the increased Zn content. The crystallization of the films was enhanced with increasing sulfide content. FESEM indicated that uniform size and quite good dispersibility were achieved at Zn/S molar ratio of 1/2. The average transmittance of the films was above 79% in the visible range, and the direct optical bandgap was enhanced from 3.2 eV to 3.56 eV by increasing the sulfide content in the film. Also, the highest refractive index and lowest extinction coefficient corresponded to the film obtained at Zn/S = 1/2. In addition, increasing the sulfide content affected the dispersion parameters (oscillator energy and dispersion energy), real and imaginary parts of the dielectric constant, and energy loss. It was observed that the minimum volume energy loss

Table III. Electrical parameters of sol–gel-derived thin films obtained using different Zn/S molar ratios

Zn/S	ρ (Ω cm)	n (cm^{-3})	μ (cm^2/V s)	Type
2/1	7.78E + 04	8.86E + 12	9.05	n
1/1	9.52E + 04	4.38E + 12	15.00	n
1/2	1.99E + 03	5.89E + 13	53.20	n

and surface energy loss were obtained for the Zn/S = 1/2 thin film. All samples exhibited *n*-type conductivity, and the carrier concentration and mobility of the films improved with increasing S/Zn ratio in the solution. The PL spectra for the nanocrystalline ZnS films were monitored at two excitation wavelengths, viz. 245 nm and 356 nm. The near-band-edge (NBE) emission showed a blue-shift as the S content was increased, confirming the broadening of the bandgap of the films. Also, the blue emission peaks centered at 438 nm and 487 can be attributed to interstitial S atoms, surface states, and zinc vacancies.

ACKNOWLEDGEMENTS

The authors would like to acknowledge University of Guilan Research Council for support of this work.

REFERENCES

1. C.B. Murray, C. Kagan, and M. Bawendi, *Annu. Rev. Mater. Res.* 30, 545 (2000).
2. V.I. Klimov, A. Mikhailovsky, S. Xu, A. Malko, J. Hollingsworth, C. Leatherdale, H.-J. Eisler, and M. Bawendi, *Science* 290, 314 (2000).
3. Q. Xiong, G. Chen, J. Acord, X. Liu, J. Zengel, H. Gutierrez, J. Redwing, L. Lew Yan Voon, B. Lassen, and P. Eklund, *Nano Lett.* 4, 1663 (2004).
4. K. Roy Choudhury, Y. Sahoo, and P.N. Prasad, *Adv. Mater.* 17, 2877 (2005).
5. N.K. Allouche, T.B. Nasr, N.T. Kamoun, and C. Guasch, *Mater. Chem. Phys.* 123, 620 (2010).
6. S. Tec-Yam, J. Rojas, V. Rejón, and A. Oliva, *Mater. Chem. Phys.* 136, 386 (2012).
7. H. Lekiket and M. Aida, *Mater. Sci. Semicond. Process.* 16, 1753 (2013).
8. I. Ahemen, F. Dejene, B. Viana, P. Aschehoug, and E. Odoh, *Mater. Chem. Phys.* 184, 250 (2016).
9. W. Liu, *Mater. Lett.* 60, 551 (2006).
10. S. Scott and H. Barnes, *Geochim. Cosmochim. Acta* 36, 1275 (1972).
11. W.G. Becker and A.J. Bard, *J. Phys. Chem.* 87, 4888 (1983).
12. W. Chen, Z. Wang, Z. Lin, and L. Lin, *J. Appl. Phys.* 82, 3111 (1997).
13. A. Kole, P. Kumbhakar, and U. Chatterjee, *Appl. Phys. Lett.* 100, 013103 (2012).
14. S. Chan, S. Lok, G. Wang, Y. Cai, N. Wang, K. Wong, and I. Sou, *J. Electron. Mater.* 37, 1433 (2008).
15. O. Echendu, A. Weerasinghe, D. Diso, F. Fauzi, and I. Dharmadasa, *J. Electron. Mater.* 42, 692 (2013).
16. S. Kumar and N. Verma, *J. Electron. Mater.* 44, 2829 (2015).
17. O. Echendu and I. Dharmadasa, *J. Electron. Mater.* 43, 791 (2014).
18. N. Fathy and M. Ichimura, *Sol. Energy Mater. Sol. Cells* 87, 747 (2005).
19. R. Sahraei and S. Darafarin, *J. Lumin.* 149, 170 (2014).
20. A. Goudarzi, G.M. Aval, R. Sahraei, and H. Ahmadpoor, *Thin Solid Films* 516, 4953 (2008).
21. Y.-J. Lin and W.-S. Ni, *J. Lumin.* 172, 286 (2016).
22. H.V. Bui, V.B. Pham, S.D. Le, and N.N. Hoang, *J. Lumin.* 178, 134 (2016).
23. A. Ates, M.A. Yıldırım, M. Kundakcı, and A. Astam, *Mater. Sci. Semicond. Process.* 10, 281 (2007).
24. G.S. Lotey, Z. Jindal, V. Singhi, and N. Verma, *Mater. Sci. Semicond. Process.* 16, 2044 (2013).
25. M.M.H. Farooqi and R.K. Srivastava, *Mater. Sci. Semicond. Process.* 20, 61 (2014).
26. W. Gao, M. Cao, W. Xiao, F. Lei, J. Huang, Y. Sun, L. Wang, and Y. Shen, *Mater. Sci. Semicond. Process.* 56, 349 (2016).
27. Z.Y. Zhong, E.S. Cho, and S.J. Kwon, *Mater. Chem. Phys.* 135, 287 (2012).
28. P.U. Bhaskar, G.S. Babu, Y.K. Kumar, Y. Jayasree, and V.S. Raja, *Mater. Chem. Phys.* 134, 1106 (2012).
29. A. Wei, J. Liu, M. Zhuang, and Y. Zhao, *Mater. Sci. Semicond. Process.* 16, 1478 (2013).
30. H. Ke, S. Duo, T. Liu, Q. Sun, C. Ruan, X. Fei, J. Tan, and S. Zhan, *Mater. Sci. Semicond. Process.* 18, 28 (2014).
31. L.-X. Shao, K.-H. Chang, and H.-L. Hwang, *Appl. Surf. Sci.* 212, 305 (2003).
32. S. Yano, R. Schroeder, B. Ullrich, and H. Sakai, *Thin Solid Films* 423, 273 (2003).
33. X. Fang, T. Zhai, U.K. Gautam, L. Li, L. Wu, Y. Bando, and D. Golberg, *Prog. Mater. Sci.* 56, 175 (2011).
34. T. Safeera, N. Johns, E. Anila, A.I. Martinez, P. Sreenivasan, R. Reshmi, M. Sudhanshu, and M. Jayaraj, *J. Anal. Appl. Pyrolysis* 115, 96 (2015).
35. I.Y. Bu, *J. Lumin.* 134, 423 (2013).
36. M. Nilkar, F. Ghodsi, and A.A. Ziabari, *Appl. Phys. A* 118, 1377 (2015).
37. I. Khan and I. Ahmad, *Int. J. Quantum Chem.* 113, 1285 (2013).
38. Z. Wen-Chena, L. Weia, and W. Shao-Yia, *J. Lumin.* 81, 149 (1999).
39. J.A. Tossell, *Inorg. Chem.* 16, 2944 (1977).
40. M. Safari, Z. Izadi, J. Jalilian, I. Ahmad, and S. Jalali-Asadabadi, *Phys. Lett. A* 381, 663 (2017).
41. M. Ashokkumar and S. Muthukumaran, *Opt. Mater.* 37, 671 (2014).
42. S. Kumar, H. Jeon, T. Kang, R. Singh, J. Sharma, and R.K. Choubey, *J. Mater. Sci. Mater. Electron.* 26, 3939 (2015).
43. K. Raja, P. Ramesh, and D. Geetha, *Spectrochim. Acta Part A* 131, 183 (2014).
44. D.A. Reddy, C. Liu, R. Vijayalakshmi, and B. Reddy, *J. Alloys Compd.* 582, 257 (2014).
45. S. Kawar and B. Pawar, *J. Mater. Sci. Mater. Electron.* 21, 906 (2010).
46. R. Swanepoel, *J. Phys. E Sci. Instrum.* 16, 1214 (1983).
47. F. Jenkins and H. White, *Fundamentals of Optics*, 4th ed. (New York: McGraw-Hill, 1973), p. 479.
48. W. Daranfed, M. Aida, A. Hafdallah, and H. Lekiket, *Thin Solid Films* 518, 1082 (2009).
49. J. Tauc, *Amorphous and Liquid Semiconductors*, 1st ed. (New York: Plenum, 1974).
50. M. DrDomenico Jr. and S. Wemple, *J. Appl. Phys.* 40, 720 (1969).
51. A. Walton and T. Moss, *Proc. Phys. Soc.* 81, 509 (1963).
52. A.A. Ziabari and F. Ghodsi, *Sol. Energy Mater. Sol. Cells* 105, 249 (2012).
53. M. Cardona and Y.Y. Peter, *Fundamentals of Semiconductors* (New York: Springer, 2005).
54. D. Denzler, M. Olschewski, and K. Sattler, *J. Appl. Phys.* 84, 2841 (1998).
55. L. Yang, Y. Tang, and S. Zhao, *J. Sol-Gel. Sci. Technol.* 53, 56 (2010).
56. X. Fang, Y. Bando, U.K. Gautam, T. Zhai, H. Zeng, X. Xu, M. Liao, and D. Golberg, *Crit. Rev. Solid State Mater. Sci.* 34, 190 (2009).
57. Q. Wu, H. Cao, S. Zhang, X. Zhang, and D. Rabinovich, *Inorg. Chem.* 45, 7316 (2006).
58. E. Mosquera and N. Carvajal, *Mater. Lett.* 129, 8 (2014).
59. Z. Li, J. Wang, X. Xu, and X. Ye, *Mater. Lett.* 62, 3862 (2008).